ADVANCED ENERGY MATERIALS
www.advenergymat.de

Novel Zwitterionic Polyurethane-in-Salt Electrolytes with High Ion Conductivity, Elasticity, and Adhesion for High-Performance Solid-State Lithium Metal Batteries

Kun Wang, Volodymyr Koverga, Namrata Maslekar, Fukang Wu, Robert Kuphl, Xingyi Lyu, Piyush Deshpande, Hanzeng Guo, Hyang Seol, Wade Degraff, Jennifer L. Schaefer, Chengcheng Fang, Tao Li, Gang Cheng, Anh T. Ngo,* and Sangil Kim**

This study presents a novel polymer-in-salt (PIS) zwitterionic polyurethane-based solid polymer electrolyte (zPU-SPE) that offers high ionic conductivity, strong interaction with electrodes, and excellent mechanical and electrochemical stabilities, making it promising for high-performance all solid-state lithium batteries (ASSLBs). The zPU-SPE exhibits remarkable lithium-ion (Li^+) conductivity (3.7×10^{-4} S cm^{-1} at 25 °C), enabled by exceptionally high salt loading of up to 90 wt.% (12.6 molar ratio of Li salt to polymer unit) without phase separation. It addresses the limitations of conventional SPEs by combining high ionic conductivity with a Li^+ transference number of 0.44, achieved through the incorporation of zwitterionic groups that enhance ion dissociation and transport. The high surface energy (338.4 J m^{-2}) and elasticity ensure excellent adhesion to Li anodes, reducing interfacial resistance and ensuring uniform Li^+ flux. When tested in Li||zPU||$LiFePO_4$ and Li||zPU||S/C cells, the zPU-SPE demonstrated remarkable cycling stability, retaining 76% capacity after 2000 cycles with the $LiFePO_4$ cathode, and achieving 84% capacity retention after 300 cycles with the S/C cathode. Molecular simulations and a range of experimental characterizations confirm the superior structural organization of the zPU matrix, contributing to its outstanding electrochemical performance. The findings strongly suggest that zPU-SPE is a promising candidate for next-generation ASSLBs.

1. Introduction

The commercialization of lithium batteries (LBs) marked a significant milestone in the evolution of energy storage technologies, powering a variety of applications, including portable electronic devices, electric vehicles, and large-scale energy storage.[1] Lithium metal batteries (LMBs) are favored for their high energy density, high working voltage, excellent cycling life, and low self-discharge rate.[2] Despite these advantages, conventional LMBs that employ organic liquid electrolytes possess significant safety challenges, including uncontrollable side reactions, lithium (Li) dendrite formation, and high flammability.[3] These safety issues have restricted a broader deployment of LMBs, prompting increased demand for safer and more stable alternatives. All-solid-state LBs (ASSLBs) emerge as a promising solution, offering enhanced battery safety and potentially improved cycling life.

Inorganic solid-state electrolytes (IEs) are promising candidates for ASSLBs

---

K. Wang, V. Koverga, N. Maslekar, F. Wu, H. Guo, W. Degraff, G. Cheng,
A. T. Ngo, S. Kim
Department of Chemical Engineering
University of Illinois at Chicago
Chicago, IL 60607, USA
E-mail: gancheng@uic.edu; anhngo@uic.edu; skim@uic.edu

The ORCID identification number(s) for the author(s) of this article can be found under https://doi.org/10.1002/aenm.202405676

DOI: 10.1002/aenm.202405676

R. Kuphl, C. Fang
Department of Chemical Engineering and Materials Science
Michigan State University
East Lansing, MI 48824-1226, USA

X. Lyu, T. Li
Department of Chemistry and Biochemistry
Northern Illinois University
DeKalb, IL 60115, USA

P. Deshpande, J. L. Schaefer
Department of Chemical and Biomolecular Engineering
University of Notre Dame
Notre Dame, IN 46556, USA

H. Seol
ZPore, LLC.
Wilmette, IL 60091, USA

due to their high lithium-ion (Li^+) conductivity, high cation selectivity, superior electrochemical stability, thermal stability, and ability to suppress dendrite growth.[4] Nevertheless, their full adoption in LMBs has been hampered by inherent brittleness and fragility, coupled with poor interfacial compatibility with electrodes.[3] In contrast, solid polymer electrolytes (SPEs) offer improved flexibility and elasticity, better interfacial contact with electrodes, and ease of processing, which have persistently drawn significant interest in the field.[5] However, conventional SPEs suffer from low room-temperature ionic conductivity and low cation selectivity ($t^+ < 0.2$).[6] Numerous modifications have been proposed to improve the electrochemical properties of conventional SPEs, such as incorporating inorganic or metal-organic fillers, adding plasticizers, copolymerization, and polymer blending.[7] Despite these efforts, achieving all the desired characteristics of solid electrolytes in traditional salt-in-polymer SPEs (SIP-SPEs), with typical Li salt mass loading < 50%,[1b,8] remains a significant challenge, particularly due to low ionic conductivity.[2] The design of SIP-SPEs typically relies on polymers that dissolve ionic salt through polar groups and transport Li^+ vehicularly through the segmental motion of the polymer. However, this solvation and ion transport process in SIP-SPEs has inherent flaws, including limited metal cation transport due to the slowed cation motion caused by strong cation-polymer coordination.

To address the low ionic conductivity issue of SIP-SPEs, polymer-in-salt SPEs (PIS-SPEs), with > 50% of Li salt mass loading, have been investigated, within which a Li^+ hopping transport mechanism contributes to the ionic conductivity.[9] In PIS-SPEs, the high loading of Li salts promotes the formation of salt aggregates, enabling metal ions to diffuse through interconnected anion aggregates, while the polymer provides mechanical stability. This design can greatly enhance Li^+ diffusion by decoupling metal-ion motions from the polymer dynamics (e.g., segmental motion, chain relaxation).[10] Previous efforts primarily employed traditional polymers such as PEO,[11] PAN,[12] or PVDF,[13] which exhibit unsatisfactory ionic conductivity and LMB performance at room temperature due to an unoptimized balance between mechanical, chemical, electrochemical stabilities, interaction with electrodes, and ionic conductivity. This limitation hinders the ability to achieve long-term, stable cycling at room temperature. Thus, there is a clear demand to explore new chemistries for efficient side-chain solvation decoupling and anion-trapping strategies, and a deeper understanding of ion transport mechanisms in ion-conducting polymers to meet the diverse performance requirements of SPEs.

To address the challenges of conventional SPEs, researchers have proposed zwitterionic (ZI) polymer electrolytes. ZIs have been widely used as additives to conventional ASSLBs to improve ion diffusivity.[14] ZI polymers are defined as bearing an equimolar number of homogenously distributed anionic and cationic groups along their polymer chains.[15] Although charge-neutral, ZI polymers possess a large dipole moment and can interact with ions, promoting ion dissociation and facilitating ion transport.[16] The developed ZI polymer electrolytes primarily involve the polymerization or copolymerization of ZI methacrylate. The resulting ZI polymer electrolytes exhibit higher ionic transport properties than conventional SPEs, albeit not yet at the desired levels.[17] Consequently, a design of solid-state ZI polymer electrolytes that meets the comprehensive performance criteria of ASSLBs is still needed.

In this study, we introduce a novel PIS-SPE based on ZI polyurethane SPE (zPU-SPE) for ASSLBs that addresses the limitations of conventional SPE materials, such as low ionic conductivity, poor contact with electrodes, and limited mechanical and electrochemical stability. We synthesized zPU [i.e., poly((diethanolamine ethyl acetate)-co-(1,6-diisocyanatohexane))] and demonstrated its capability to host up to a high Li^+/ZI mole ratio of 12.6 (90 wt.%) of lithium bis(trifluoromethanesulfonyl)imide (LiTFSI) without the phase separation of Li salt and polymer. The ionic conductivity of zPU-SPE at 25 °C is 3.7×10^{-4} S cm^{-1}, two orders of magnitude greater than that (1.9×10^{-6} S cm^{-1}) of poly(ethylene oxide) (PEO) SPE ($Li^+/EO = 1/16$). Moreover, the high surface energy of zPU-SPE minimizes interfacial resistance. We evaluated the cycling performance using a Li||zPU||$LiFePO_4$ cell (1 C at 25 °C) and Li||zPU||S/C (0.3C at 25 °C). Both LB cell with zPU-SPE demonstrates remarkable cycle stability, with 77% capacity retention after 2000 cycles for the $LiFePO_4$ cathode and 84% capacity retention after 300 cycles for the S/C cathode, while maintaining ≈100% coulombic efficiency. We also conducted atomistic molecular modeling to investigate the solvation of Li salts and Li salt-zPU interactions, which provide insights into Li^+ transport within the zPU polymer matrix. Furthermore, we employed small-angle X-ray scattering (SAXS) to examine the structural organization of the zPU-SPE matrix and its correlation with ion conductivity. Our work aims to guide the design of novel polymer electrolytes capable of overcoming the trade-offs associated with ion-conducting polymers.

2. Results

2.1. Fabrication of zPU-SPE

Figure 1a illustrates a schematic chemical structure of the synthesized zPU. In zPU, the high density of inter- and intramolecular hydrogen bonding between the urethane groups, coupled with the stack of rigid 1,6 Diisocyanatohexane (HDI) segments, contributes significantly to the thermal and mechanical properties of the zPU. The carboxybetaine ZI group can effectively solvate LiTFSI, enabling fast Li^+ diffusion. Its chemistry maximizes ion mobility by providing notable coulombic interactions to dissociate salt ion pairs while balancing ion solvation and dissociation,[18] avoiding Li^+ trapping and low diffusivity. Moreover, the carboxybetaine group has been reported to have higher compatibility with the Li anode compared to the sulfobetaine and phosphoric betaine groups.[18b] As illustrated in Figure S1a (Supporting Information), carboxybetaine zPU was synthesized via polycondensation of the ZI precursor (DEAEA) with HDI,

---

V. Koverga, T. Li
X-ray Science Division
Argonne National Laboratory
Lemont, IL 60439, USA

A. T. Ngo
Material Science Division
Argonne National Laboratory
Lemont, IL 60439, USA

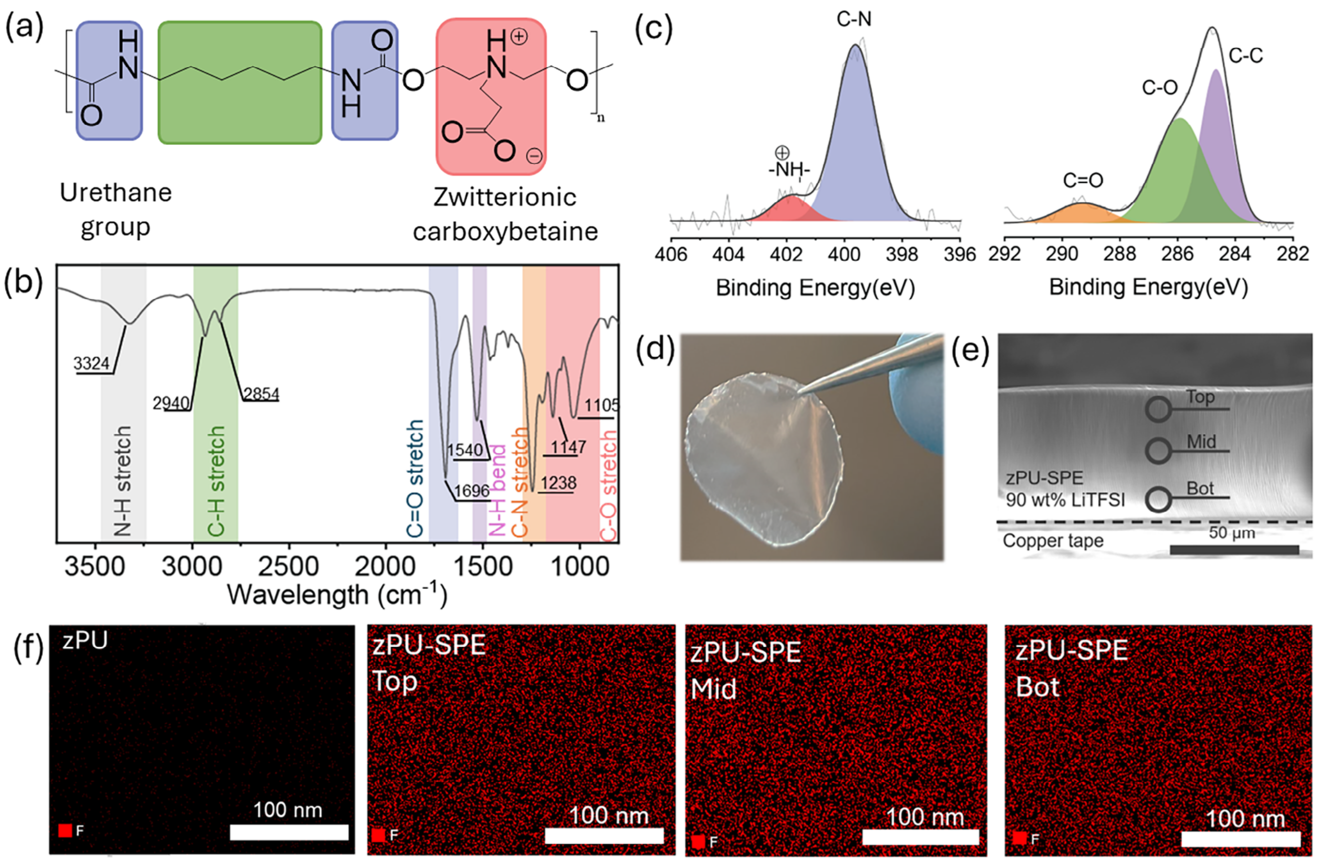

Figure 1. a) Molecular structures of zPU. b) FT-IR spectroscope of zPU. c) XPS curves of zPU. d) Picture of fabricated zPU-SPE. e) Cross-section SEM image of zPU-SPE. f) SEM-EDX images of zPU and zPU-SPE with 90 wt.% LiTFSI loading. The top, mid, and bot indicate three different areas of the cross-section of the zPU-SPE.

followed by the hydrolysis of the ethyl ester to generate ZI carboxybetaine groups. DEAEA was selected as both a chain extender and a ZI precursor. The successful synthesis of carboxybetaine zPU with a molecular weight of ≈10k (Figure S1b, Supporting Information) was confirmed by ^{1}H NMR and ^{13}C NMR, as shown in Figure S1c,d (Supporting Information). The chemical composition of zPU was characterized using ATR-FTIR analysis (Figure 1b). Notable absorption bands for N—H stretching, C—H stretching, C=O stretching, C—O—C stretching, and N—H bending were observed at 3324, 2940–2854, 1696, 1105–1147, and 1540 cm^{-1}, respectively. Additionally, the XPS survey scan spectrum of the zPU showed O1s, N1s, and C1s peaks (Figure 1c). The N1s peak at 399.8 eV corresponds to the C—N bonds in the urethane group, while the peak at 402.0 eV can be attributed to the quaternary amine in the zwitterionic carboxybetaine group. The C1s spectrum exhibits three characteristic peaks at 284.4, 285.6, and 289.1 eV, which are assigned to the carbon atoms in saturated hydrocarbons (—C—C—), carbon atom bonding to oxygen (—C—O—), and carbon atoms in the urethane and carboxybetaine groups (—C = O—), respectively. These results, corroborated by the ATR-FTIR analysis, confirm the successful synthesis of the zPU incorporating carboxybetaine ZIs.

The zPU-SPE was prepared by impregnating a solution of LiTFSI into zPU film, and subsequently removing the solvent through vacuum drying. The absence of solvent residues in zPU-SPE was further verified using TGA, with zPU as a reference (Figure S1e, Supporting Information). The derivative thermogravimetry (DTG) curves of both zPU and zPU-SPE confirm that the prepared zPU-SPE contains minimal volatile solvent residues. In this study, we used LiTFSI because it is a highly labile salt that can easily dissociate in the presence of ion-solving functionalities.[17d] Figure 1d shows a photo of the prepared zPU-SPE used in the fabrication of ASSLB. Of note, our ASSLB fabrication process with zPU-SPE does not require complicated in situ polymerization or post-functionalization during battery assembly, thereby enabling roll-to-roll assembly of SPE-based ASSLB. Figure 1e,f presents the SEM images of the cross-section of the prepared zPU-SPE (90 wt.% of LiTFSI loading). Excess salt loading or insufficient solvation of salt in polymer could lead to salt precipitation and poor-ion-conducting salt crystal phase.[19] To examine the homogeneity of LiTFSI dispersion in the zPU matrix, we assessed the distribution of elements using SEM-EDX. For the zPU polymer without LiTFSI addition, no fluorine (F) signal was detected due to the absence of F in the zPU polymer chain. The SEM-EDX cleary showed a uniform F (from LiTFSI) distribution across both surfaces and the middle regions of the zPU-SPE after impregnation of LiTFSI. Furthermore, no micron-scale phase segregation was observed within the zPU-SPE. Carbon (C), nitrogen (N), and sulfur (S) also exhibited a homogenous distribution (Figure S2, Supporting Information). These

SEM-EDX images suggest a uniform distribution of LiTFSI within the zPU-SPE.

It should be noted that PU is generally considered as a phase separation material. This is due to the inherent structure of PU, which typically consists of hard and soft segments, the interplay of which can give rise to microphase separation.[20] This characteristic structure of typical PU-based SPEs results in the formation of a rigid phase, generally associated with lower ionic conductivity. Nonetheless, this is balanced by the existence of a flexible phase in PUs, often contributing to enhanced ion transport.[21] Interestingly, such dual-phase morphology was absent in zPU-SPE, attributed to its short diols and diisocyanates. Moreover, our zPU-SPE is a PIS-SPE system and contains a high salt loading of up to LiTFSI/ZI ratio of 12.6 (90 wt.% of LiTFSI salt in zPU-SPE), suggesting that its ion transport mechanism greatly depends on surface diffusion through interconnected anion aggregates. It has been noted that at high Li salt loading above 50 wt.%, regional LiTFSI aggregation, and crystallization could occur, which could hinder ion transports and thereby reduce the overall ionic conductivity.[11] Nevertheless, our zPU-SPE demonstrated an exceptional capability for high LiTFSI impregnation, without showing regions of aggregated LiTFSI region even at a high salt loading of 90 wt.%.

2.2. Characterization of zPU-SPE

The adhesion between the electrolyte and Li anode significantly impacts the performance of the LMBs.[22] The improved contact between the electrode and zPU-SPE reduces interfacial resistance, facilitates a more uniform Li$^+$ concentration profile at the interface, and thus enhances Li$^+$ transport.[23] Poor adhesion at the interface during Li metal stripping is responsible for constriction resistances and hotspots that can facilitate dendrite propagation and failure. We evaluated the surface adhesion energy between zPU-SPE and Li foil using a peeling test (**Figure** 2a; Figure S3, Supporting Information). Notably, as shown in Figure 2b, the zPU-SPE demonstrated exceptional adhesion properties on Li metal, exhibiting a surface adhesion energy of 338.4 J m^{-2}. This high surface adhesion energy is ≈5 times higher than that of traditional PEO-SPE and surpasses even commercially available pressure-sensitive adhesive tapes, such as Kapton and Scotch tape. Such high adhesion can lead to more uniform Li$^+$ concentration profiles at the zPU-SPE and Li anode interface and well-distributed current density.[22a] Both experiments and simulation studies have shown that enhanced adhesion can effectively suppress the growth of Li dendrite, which is highly desirable in ASSLBs.[22a,24] Upon contact with the Li foil surface, the charged ZIs in zPU-SPE generate strong electrostatic attraction and Van der Waals interactions, thereby enhancing the swift and strong bonding of zPU-SPE to the Li anode.[22b,25] Additionally, the higher density of hydrogen bonding from the urethane groups contributes to the strong adhesion and cohesion near the interface.[25a] The robust adhesive property also benefits from the elasticity of zPU-SPE. The soft thermoplastic nature of zPU-SPE can increase the contact area with the Li metal surface due to the deformation of zPU-SPE during contact and compression.[25a] The SEM image of the LFP cathode infiltrated with zPU-SPE (Figure 2c) reveals a uniform interfacial contact, free of voids or delamination. This robust interface results from the high surface adhesion energy of zPU-SPE, which ensures efficient wetting and bonding. Such intimate contact minimizes interfacial resistance and enables stable ion transport, confirming the mechanical compatibility of zPU-SPE with the cathode and its potential for long-term cycling stability in ASSLBs.

In addition to the excellent interfacial adhesion, the self-healing properties of zPU-SPE can also help to extend the cycling life in ASSLBs. Li deposition generally causes cracks in traditional SPEs during repeated insertion and extraction of Li$^+$ in the charge and discharge process, which results in shortening the lifetime of ASSLBs.[26] In comparison, zPU-SPE possesses self-healing properties through reversible, non-covalent bonds, which extend the ASSLB lifetime and improve the cycling stability after crack or deformation.[27] As shown in Figure 2d, the zPU-SPE can recover to its original shape within 10 min after being cut in half, as the gap gradually disappears. The zPU-SPE is an autonomous, self-repairing material realized through its supramolecular networks fabricated by non-covalent interactions, including hydrogen bonding and dipole-dipole interactions, as illustrated in Figure 2e. Upon deformation or cracking, the ZI carboxybetaine groups on the broken interface pair again via a dipole-dipole interaction to return to the original state.[28] Meanwhile, hydrogen bonds also form between the urethane groups.[29] The two kinds of forces work together to achieve excellent self-healing properties. Additionally, DSC shows that the zPU has a low glass transition temperature of −8 °C (Figure S4, Supporting Information). Such a glass transition temperature is below the ambient temperature, which helps with the fast chain movement and the self-healing of zPU-SPE.[27,30]

The electrochemical stability of zPU-SPE and PEO-SPE was investigated using linear sweep voltammetry (LSV) (Figure S5, Supporting Information). LSV measurements were conducted at room temperature in SS||SPE||Li cells with a scan rate of 0.1 V min^{-1}. As shown in the anodic scan, the onset of oxidation current for zPU-SPE was observed ≈4.25 V vs. Li/Li$^+$. This current can be attributed to the oxidative decomposition of zPU by the strong bis(trifluoromethanesulfonyl)imide acid (HTFSI) formed from LiTFSI at voltages above 4.2 V vs. Li/Li$^+$.[31] The oxidative stability of zPU-SPE was comparable to that of traditional PEO-SPE. The voltage window observed in the LSV suggests that zPU-SPE is electrochemically stable and suitable for application in Li/LiFePO$_4$ and Li/S cells. Although the oxidative stability of zPU-SPE is comparable to that of traditional PEO-SPE, further improvements are necessary for ASSLB applications at high voltage. Ongoing research focuses on exploring various lithium salts, diols, and hard segments to enhance the performance of zPU-SPE under high-voltage conditions.

Figure 2f represents the ionic conductivity properties of the zPU-SPE in comparison to PEO-SPE at different temperatures. The results show that the zPU-SPE predominantly follows the Arrhenius model within the temperature window of 20—90 °C, whereas the PEO-SPE complies with the Vogel–Falcher–Tammann (VFT) model. The non-linearity behavior in VFT model indicates that ion transport in the PEO-SPE is assisted by the polymer segmental motion.[32] In comparison, the Arrhenius-like relationship in zPU-SPE represents the fact that the Li$^+$ transport does not arise from the molecular motion of the polymer host. Instead, the Li$^+$ transport in the zPU-SPE

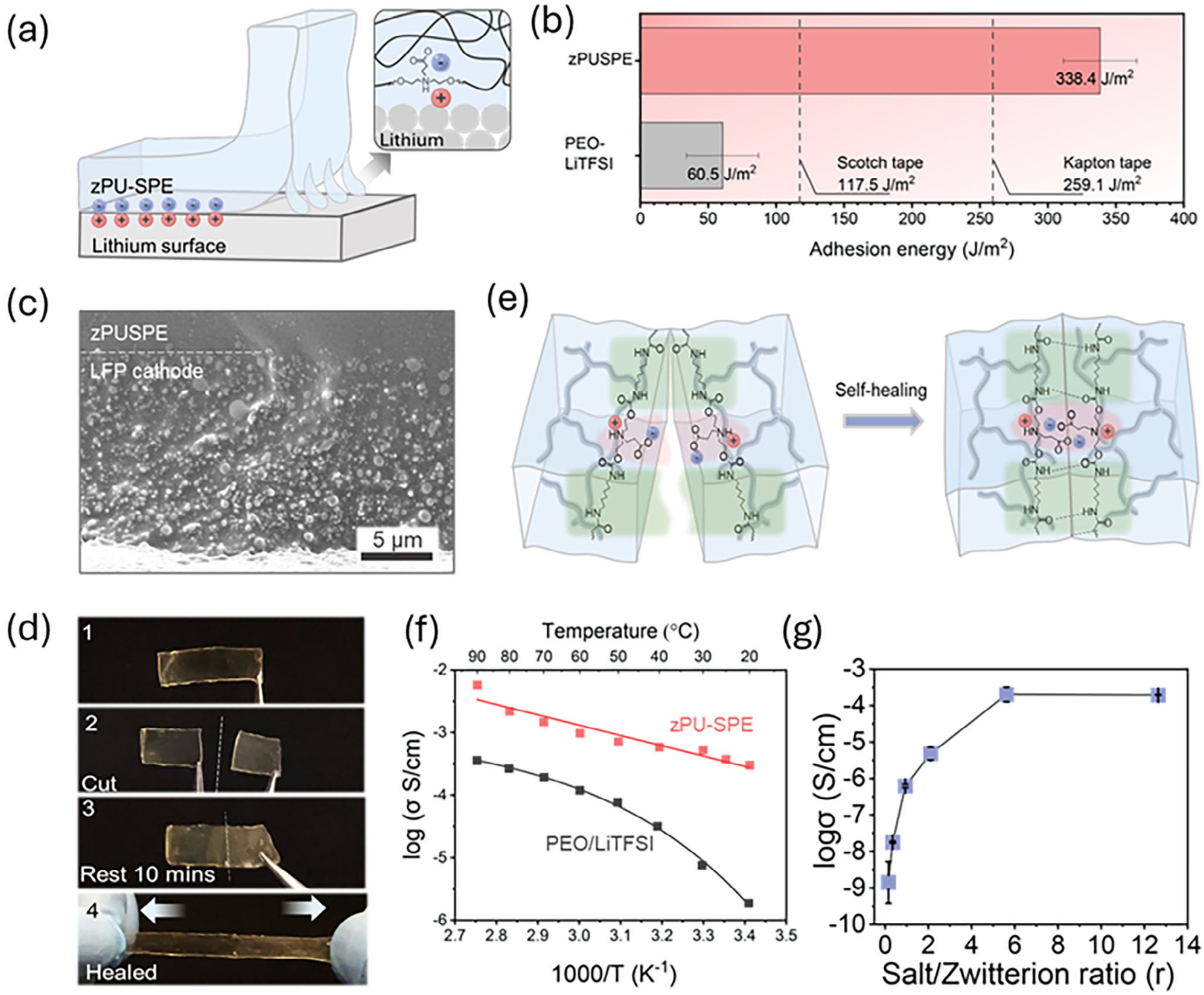

Figure 2. a) Illustration of the adhesion mechanism of zPU-SPE on the lithium metal surface. b) Surface adhesion energy of zPU-SPE with lithium metal in comparison to traditional PEO-SPE, Scotch tape, and Kapton tape. c) Cross-section image of the zPU-SPE infiltrated LFP cathode. d) Photography of the seal-healing process of zPU-SPE. e) Illustration of the healing mechanism of zPU-SPE. f) The temperature dependence of ionic conductivity for zPU-SPE compared with PEO-LiTFSI. g) Ion conductivity values as a function of LiTFSI/ZI molar ratio.

can be associated with ions jumping to the nearest vacant sites (ion hopping mechanism), as in PIS-SPE and inorganic ceramic electrolytes.[32] The behavior of ionic conductivity with increasing temperature in the zPU-SPE points to a distinction transport mechanism different from traditional PEO-based SPEs. Compared to the PEO-SPE, the zPU-SPE exhibits an ionic conductivity ≈200 times higher (3.7×10^{-4} S cm^{-1} vs. 1.9×10^{-6} S cm^{-1}) at room temperature. Furthermore, the ionic conductivity of the zPU-SPE significantly exceeds that of previously reported thermoplastic PU-SPEs without ZI moieties.[33] The activation energy of ionic conductivity (E_a) was found to be 0.14 eV for the zPU-SPE, a noteworthy finding given that SPEs typically exhibit larger E_a values. The lower E_a for the zPU-SPE implies a distinctive and efficient ion transport mechanism,[34] which we attribute to the attractive ZI group and Li$^+$. When ZI is combined with LiTFSI, they aid in the dissociation of Li$^+$ from the Li$^+$/TFSI$^-$ cluster, subsequently leading to an increase in both the number and average mobility of Li$^+$ in the zPU-SPE matrix. Moreover, we systematically studied the changes in ion conductivity of zPU-SPE at various LiTFSI/ZI molar ratios (r): 0.2 (10 wt.% LiTFSI), 0.4 (20 wt.% LiTFSI), 0.9 (40 wt.% LiTFSI), 2.1 (60 wt.% LiTFSI), 5.6 (80 wt.% LiTFSI), and 12.6 (90 wt.% LiTFSI). As shown in Figure 2g, the results show an increase in ionic conductivity with increasing LiTFSI/ZI ratios from 0.2 to 12.6. Previous work has also reported such a monotonous increase of ionic conductivity in ZI polymers throughout a wide range of salt concentrations.[17d] Although an $r = 12.6$ results in the highest ionic conductivity, to balance between ionic conductivity and the mechanical property, we adopted $r = 5.6$ (80 wt.% LiTFSI) in most of the ASSLB assembly and evaluation.

In battery applications, it is critical to maximize $t_{Li}{}^+$, which represents the proportion of current carried by Li$^+$ over all ions in the electrolyte. Traditional SPEs prepared using organic liquid electrolytes with LiTFSI typically exhibit a $t_{Li}{}^{+}$ less than 0.3.[35] As a result, a high ratio of the movable counter anion (e.g., TFSI$^-$) induces greater susceptibility to concentration polarization. These mobile anions can disrupt with the Li$^+$ movement and interfere with uniform Li$^+$ deposition on the electrode surface, thereby exacerbating Li dendrite growth.[36] We performed chronoamperometry tests on the zPU-SPE at 30 °C, and a calculated $t_{Li}{}^{+}$ was 0.44 (Figure S6, Supporting Information). As shown in Figure S7 (Supporting Information), the performance of our zPU-SPE is slightly better than the universal upper bound reported by Balsara and co-workers for polymer electrolytes.[37] The higher $t_{Li}{}^{+}$ for the zPU-SPE is beneficial in fostering a more homogeneous Li$^+$ flow and suppressing the formation of Li dendrites. In traditional dual ion-conducting electrolytes, Li$^+$ is typically surrounded by solvent molecules, solvation groups bound to the polymer, or anion clusters, which can result in slower motion of Li$^+$ compared to anions. However, we speculate on a distinctive ion-transport mechanism in the zPU-SPE. In the zPU-SPE, the attractive interaction between the ZI group and the Li$^+$ facilitates the enhanced dissociation of the Li$^+$/TFSI$^-$ cluster aggregation. Consequently, a greater number of free Li$^+$ are released for rapid diffusion, resulting in a higher $t_{Li}{}^{+}$.[34,38] While two SPEs have been previously reported with higher ionic conductivity over 10^{-3} S/cm and transference number over 0.75 with good cycling stabilities up to 1000 cycles in full LMB, their application on LMBs could be limited due to the requirement for in situ polymerization in a LMB[22c] or its restricted use as a protective interlayer between the anode and SPE.[39]

2.3. Salt Solvation and Ion Transportation Mechanisms in zPU-SPE

The relatively high Li salt concentration in typical SPEs hinders the dissociation of Li salt and promotes the formation of ion clusters due to less oxygen solvation sites in the polymer (e.g., PEO), which significantly decreases ion conductivity.[40] To understand the excellent miscibility of zPU with a high amount of Li salt and the high ionic conductivity even at a high Li/ZI mole ratio, the effect of Li salt (i.e., LiTFSI) solvation in zPU-SPE on ion conductivity was investigated by employing molecular dynamics (MD) simulation, SAXS, and Raman spectroscopy. SAXS was first conducted to validate the predictive ability of MD calculations and to probe the long-range structural arrangement in zPU-SPE. As shown in **Figures** 3a and S8a (Supporting Information) (the full LiTFSI concentration range), the simulated curve and the experiment are in high qualitative agreement, allowing the origin of the charge ordering peak to be established. A noticeable peak at ≈14.73 nm^{-1} maintained predominant intensity across the entire concentration range, corresponding to the distance between the neighboring atoms of either the same anion or neighboring anions within the polymer. Meanwhile, a preceding shoulder at ≈8.27 nm^{-1} which grows rapidly with increasing Li salt concentration. The peak located at lower q values on the SAXS profiles is attributed to the formation of a long-range ordered electrostatic network between positively and negatively charged ions (charge ordering peak).[41] The increasing intensity of the shoulder, followed by peak formation, can be attributed to the growing probability of interionic correlation excluded from the solvation shell as the Li salt concentration increases.[41a] Since the first peak at 8.27 nm^{-1} corresponds to a characteristic distance of $d = 2\pi / q \approx 0.73$ nm, it aligns well with the periodicity of the corresponding radial distributions of Li$^+$•••Li$^+$, TFSI$^-$•••TFSI$^-$, and Li$^+$•••TFSI$^-$ across the entire concentration range (Figure S8b, Supporting Information). The asynchronous oscillation of these distributions can be interpreted as alternate mutual screening of oppositely charged ions to establish local charge neutrality.

To understand the solvation structure of Li salt and zPU polymer and its effect on ionic conductivity, the radial distributions were analyzed between the representative atomic sites of all the zPU-SPE constituents (Figure 3b). Precise examination of interionic Li$^+\cdots$TFSI$^-$ interactions, characterized by the oxygen atom as the strongest interaction center in TFSI$^-$, exhibited a sharp peak at ≈0.20 nm with a minimum at 0.26 nm. This indicates relatively strong interionic interactions, which are typical for liquid organic electrolytes, ionic liquids, and SPEs containing Li salts with triflimidate anions. Li$^+$ also shows competitive solvation by zPU, particularly evident for Li$^+\cdots$O pairs involving urethane (UR) and carboxybetaine (zPU$^-$) groups. The first peak for Li$^+\cdots$zPU$^-$(0.18 nm) and Li$^+\cdots$UR (0.19 nm) occurs at slightly shorter distances than for Li$^+\cdots$TFSI$^-$, suggesting a stronger preference for Li$^+$ localization toward zPU$^-$. The extension of the solvation shell differs more for these pairs than for their interaction strength. The minimum in the radial distribution for zPU$^-$ is at 0.25 nm, while for UR, it is at 0.28 nm, attributed to the higher electronegativity in zPU$^-$, driven by its ZI nature and large dipole moment. To study the role of the nitrogen atom of the carboxybetaine group (zPU$^+$) as a region of lower electron density, further investigations into TFSI$^-$ solvation and interchain interactions were conducted (Figure S9, Supporting Information). Unlike Li$^+$ interactions, radial probabilities with zPU$^+$ as the reference center show relatively complex behaviors, characterized by multiple peaks with significantly lower intensities and broader spans. The lowest peak intensity ≈0.3 nm for TFSI$^-$ indicates weak delocalized interactions with zPU$^+$. The second peak at 0.46 nm suggests proximity to the second sulfonyl group. Interchain interactions of zPU are weaker (0.27–0.28 nm) due to competition between interchain association and Li$^+$ solvation. This dispersion of electron density may cause the relatively weak interactions with UR compared to zPU$^-$.

Changes in LiTFSI content lead to variations in the position, intensity, and shape of radial distributions describing interactions between the electrolyte constituents, reflected in the alteration of the running coordination number, $cn(r)$, which signifies the coordination ability of the reference atom with respect to the observed one, calculated by integrating the distribution up to the first minima (right y-axis of Figure 3b). A notable increase in the peak intensity of $cn(r)$ for Li$^+\cdots$TFSI– from 20 to 40 wt.% LiTFSI suggests a rise in $cn(r)$ for TFSI$^-$ from 0.35 to 1.36, further increasing to 3.07 at 80 wt.% and 3.47 at 90 wt.% LiTFSI. However, the coordination ability of Li$^+$ with zPU (UR and zPU$^-$) decreases from 2.48 (Li$^+\cdots$zPU$^-$) and 0.91 (Li$^+\cdots$UR) to 0.56 and 0.17, respectively, as LiTFSI increases. Notably, the reduction in Li$^+\cdots$UR coordination remains steady up to 60 wt.% LiTFSI, then drastically decreases as LiTFSI concentration increases. This trend highlights the competition between ion aggregation and solvation with increasing salt content. As Li salt concentration

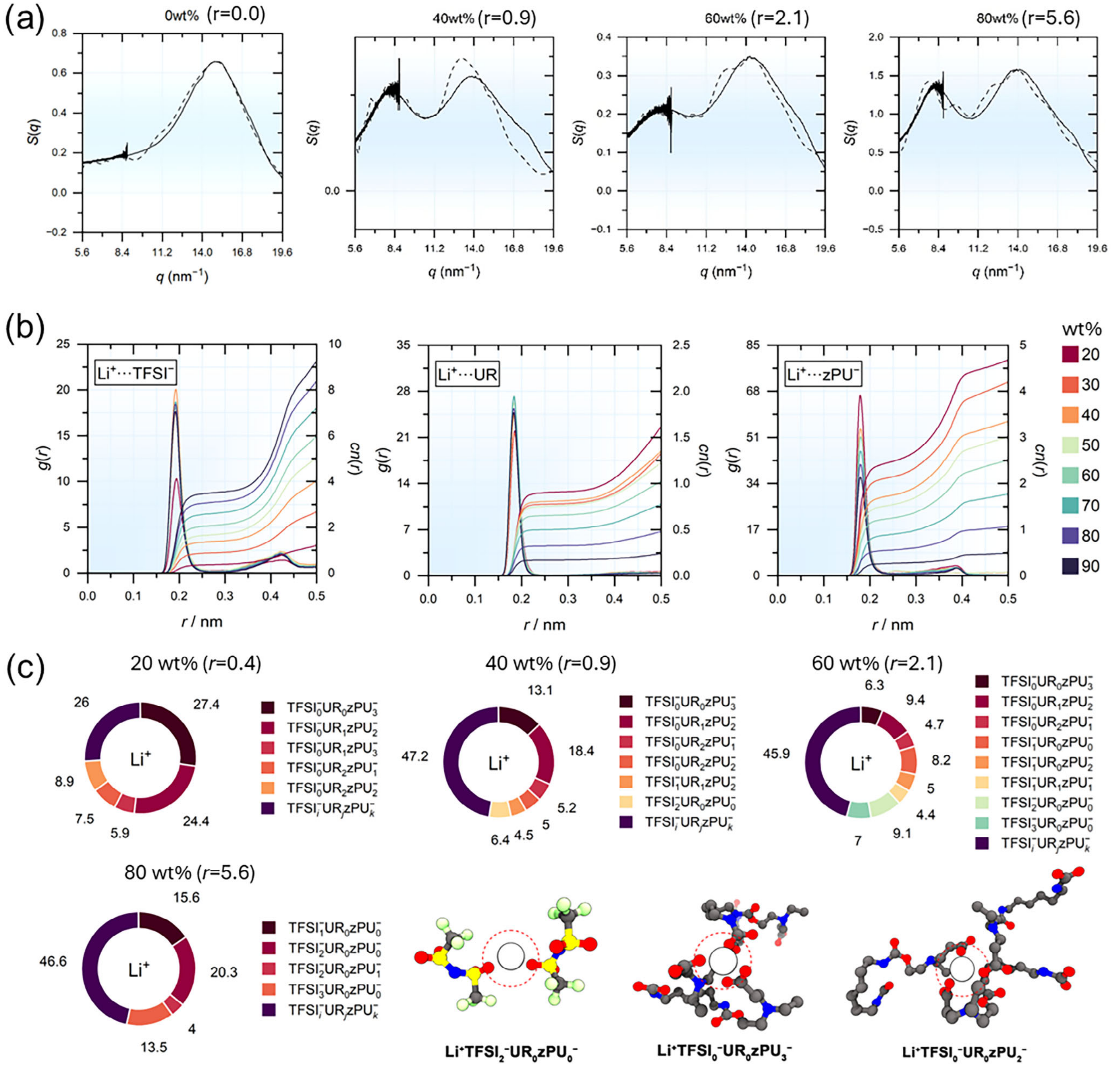

Figure 3. a) Concentration evolution of intensities from small-angle X-ray scattering measurements of zPU-SPE in comparison with the molecular simulation results of structure factor analysis as a function of scattering vector q. b) Concentration evolution of Li$^+$ and zPU solvation structure in zPU-SPE described by the radial distribution function ($g(r)$, left-hand axis), running coordination number ($cn(r)$, right-hand axis) of Li$^+$•••TFSI$^-$, Li$^+$•••UR, and Li$^+$•••zPU$^-$ interactions. c) Concentration evolution of coordination environment of Li$^+$ represented by statistical distribution of TFSI and zPU negative interaction center (the oxygen atom of urethane (UR) and carboxybetaine (zPU$^-$) group, respectively) obtained by means of MD simulation from 20 (r = 0.4) to 80 wt.% (r = 5.6) of LiTFSI. Data for the full LiTFSI concentration range (20–90 wt.% LiTFSI) are shown in Figure S10. Note that percentage distribution <4% has been merged and labeled as $TFSI_i^-UR_jzPU_k^-$. The most probable configurations are derived from the MD trajectories, with the dotted circle indicating the border of the solvation (threshold of 3.25 Å) shell used for the analysis.

increases, the aggregates become more interconnected, promoting the Li$^+$ diffusion along the surface of anion aggregates.[42] This demonstrates the enhanced ion transport mechanism of zPU-SPE, which can efficiently decouple metal-ion motion from polymer dynamics. Conversely, the first peak intensity for zPU$^+$ indicates weak coordination with TFSI$^-$ or zPU$^-$ moieties.

To further investigate the role of Li$^+$ and zPU$^+$ as key coordination centers within the zPU-SPE, a statistical analysis of their coordination environments was conducted (see Figure 3c; Figure S10, Supporting Information for solvation environment of Li$^+$ and Figure S11, Supporting Information for that of zPU$^+$). Specifically, for Li$^+$ local environment at 20 wt.% LiTFSI (r = 0.4), two predominant contributions are observed: Li^+-zPU_3^- (27.4%) and Li^+-UR-zPU_2^- (24.4%), while the presence of Li^+-$TFSI^-$ complex is less than 4%, indicating that Li^+ interacts more with polymer than with $TFSI^-$. As LiTFSI increases to 40–60 wt.% (r = 0.9–2.1), a redistribution of Li^+ occurs, with ionic and Li-zPU complexes coexist due to the gradual decrease of Li^+-zPU_3^- and Li^+-UR-zPU_2^- in favor of $Li^+TFSI_i^-$ (i = 1–3), which significantly increases beyond 60 wt.% (r = 2.1) LiTFSI content.

The transition of Li^+ redistribution at r = 0.9 – 2.1 observed in the statistical analysis was also evidenced by Raman spectroscopy. **Figure** 4a-c represent the Raman peak analysis of $TFSI^-$ anion in zPU-SPE with different LiTFSI loadings. As the LiTFSI concentration increases, the peak shifts to a higher wavenumber, indicating greater coordination between $TFSI^-$ and Li^+ (Figure 4a).[43] After the fitting of Raman peaks, the Li salt ions can be categorized into solvent-separated ion pairs (SSIP), contact ion pairs (CIP), and aggregates (AGG), as illustrated in Figure 4b. At r = 0.9–2.1, the number of $TFSI^-$ in SSIP increased to 0.76 mmol per gram of zPU-SPE with an increasing LiTFSI/ZI ratio from r = 0.2 to r = 1 (Figure 4c). When the LiTFSI/ZI mole ratio exceeds r = 1, the number of $TFSI^-$ in SSIP drops due to the saturation of ZIs by salt ions. Accompanied by the decreased number of SSIP, the number of $TFSI^-$ in CIP and AGG increases and dominates at higher salt concentrations, which is consistent with the results of MD simulation and SAXS analysis, resulting in the enhancement of Li^+ mobility and, hence, ionic conductivity. It is also notable that, with this redistribution of Li^+ coordination environment, a contribution is observed for *free* Li^+, not associated with either the anion or the polymer. Additional analysis of zPU^+ as a coordination center shows a distinct predominance of the zPU^+-zPU^- complex (67.9%), which gradually decreases with increasing LiTFSI content. A similar trend is observed for the less pronounced zPU^+-UR complex. This coordination redistribution is accompanied by the growing number of $TFSI^-$ ions in proximity to zPU^+. These MD simulation results, along with Raman analysis and the increasing intensity of the first SAXS peak, suggest a competition between Li^+ solvation, dominant up to 40–60 wt.% of LiTFSI, and ion aggregation at higher concentration (>60 wt.%). Consequently, Li^+ diffusion along the surface of anion aggregates, as well as the release of free Li^+ (>40 wt.%), not associated with ionic aggregates or zPU solvation, contributes to the significant increase in ionic conductivity of zPU-SPE.

It is well established that better salt dissociation occurs with stronger solvent-salt interactions and weaker cation-anion interactions.[44] In traditional polymer electrolytes, such dissociation is typically achieved by polymers with ion-chelating groups, such as ethereal groups.[11] Ionic transport across the polymer electrolytes can occur via either the vehicular or structural mechanism.[45] In the vehicular mechanism, the ions move with the polymer chain segments, while in the structural mechanism, the ions hop through a serial ion association-dissociation process or transport within ion clusters. At low salt loading (SIP region), strong chelation of Li^+ by chain segments makes the Li^+ transport almost exclusively vehicular. ZIs exhibit a stronger chelating effect with metal ions, as evidenced by the smaller peak distance and larger probability in the radical distribution, thereby enhancing Li salt dissociation. The effect of ZIs on increasing ionic conductivity has been observed in various PIS electrolytes, where increased ion transport is attributed to better dissociation and a higher number of carrier ions.[16c,46]

The ionic conductivity increases with an increasing salt loading in zPU-SPE, a phenomenon also observed in traditional polymers used to prepare PIS electrolytes.[11,12,35a,47] In these traditional PIS electrolytes, ionic conductivity increases until a local crystalline phase forms, typically less than 2.0 mole ratio of Li salt to polymer repeating unit, and their ion conductivity values at room temperature are $\approx 10^{-6}$ S/cm.[47b,48] The mechanism behind this increased conductivity is not fully understood so far.[44] In PIS electrolyte, the number of solvation molecules is insufficient to fully coordinate all cations and separate them from anions. Consequently, cation transport occurs via anion and solvent exchange or charged cluster diffusion, as only a small fraction of Li^+ is separated by solvent.[44] A similar solvation competition was found in zPU-SPE through the simulation and Raman studies discussed earlier. However, unlike traditional polymer electrolytes, zPU-SPE exhibits increasing ionic conductivity up to 90 wt.% of LiTFSI (r = 12.6) without crystallization. This high salt loading capacity is attributed to the strong solvation ability of the ZI groups toward both cations and anions. Additionally, in PIS region (salt loading >50 wt.%), the overall conductivity of zPU-SPE at room temperature is 1–2 orders of magnitude higher than traditional electrolytes.

The analysis of the ion cluster formation can further shed light on the relationship between ion conductivity and ion aggregate formation at high salt concentration, which could be supposed as the dominant mechanism for zPU-SPE compositional variation. A population analysis of ionic cluster formation was conducted at various LiTFSI concentrations (Figure 4d), with ion distributions in zPU-SPE visualized through representative snapshots (Figure 4e). Despite differences in spatial extension with varying LiTFSI content, a key feature across all distributions is the relatively high probability of ion pair formation and the presence of free Li^+ and $TFSI^-$ ions. At low concentrations, solvated Li^+ ions (≈73%) predominate over solvated anions (<0.5%), neutral pairs (20%), and larger aggregates (2%). As LiTFSI content increases, the probability of these aggregates rises slightly. Ion association causes initially high negatively charged ionic aggregates to extend spatially, shifting the charge balance toward neutral clusters. Interestingly, at the highest LiTFSI content, distributions shrink to smaller clusters. As the zPU-SPE saturates with LiTFSI, cluster domains expand, forming branched, positively charged ion aggregates. This potentially indicates the formation of finite-sized, positively charged clusters rather than large LiTFSI agglomerations in the zPU matrix, consistent with SAXS and SEM-EDX results.

The results of the ion cluster population analysis strongly suggest that unique ion clustering in zPU-SPE with high Li salt composition (so-called PIS electrolyte) could be a primary mechanism for its inherent high ionic conductivity. A general feature of ion clusterization is the increase in spatial extent with LiTFSI content. Along with the formation of higher-order aggregates ($n_+ n_- > 18$), the main contribution comes from free Li^+ and neutral pairs. At low LiTFSI loading, this phenomenon is due to the higher solvation of Li^+ by UR and zPU^-. However, as LiTFSI further increases, the reduction of free Li^+ is explained by the predominant ion association. The shift from neutrality in the ion aggregates toward the negatively charged clusters is due to the

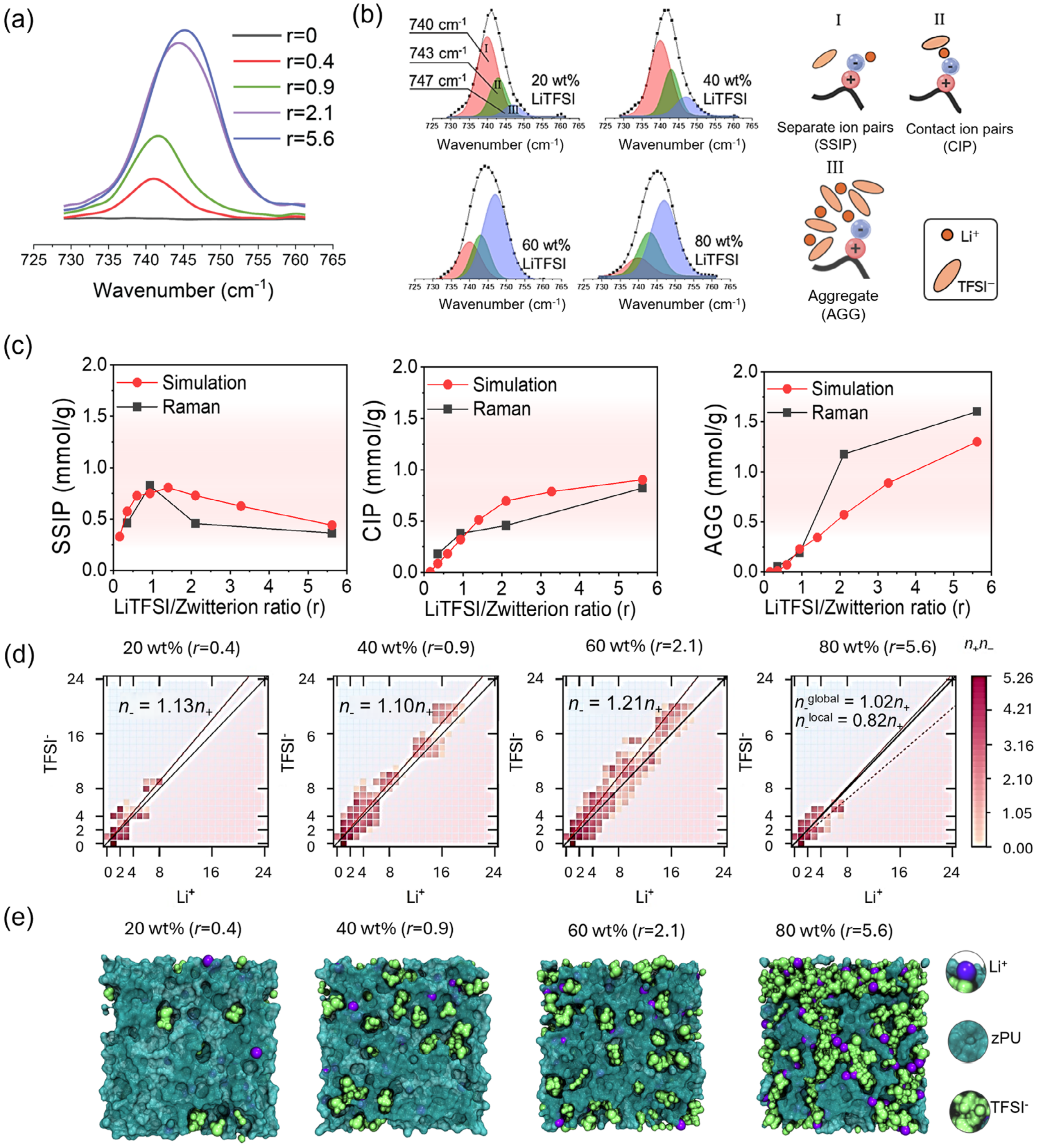

Figure 4. a) Raman spectra of zPU-SPE with different LiTFSI/ZI molar ratios. b) Raman curve peak fitting of zPU-SPE with 20 (r = 0.4), 40 (r = 0.9), 60 (r = 2.1), and 80 wt.% (r = 5.6) LiTFSI and illustration of the solvent-separated ion pairs (SSIP), contact ion pairs (CIP), and aggregates (AGG). c) Mole number of TFSI- in SSIP, CIP, and AGG per gram of zPU-SPE. d) Ion cluster population analysis of TFSI$^-$ with respect to Li$^+$ for 20, 40, 60, and 80 wt.% of LiTFSI in zPU-SPE represented in logarithmic scale. The vertical bar represents the occurrence frequency of the corresponding clusters analyzed based on the threshold distance of 3.75 Å between Li and N, O, and F atoms of TFSI$^-$. The *black* diagonal line represents the neutrality of the ion aggregates, and the *red* line fitted to the first-degree polynomial $n_- = an_+$ (where a is a fitting coefficient), represents a deviation from neutrality toward negative ($a > 1$) or positive ($a < 1$) ion rich aggregates. e) Visualization of ion distribution in zPU matrix by representative snapshot slices along Z axis of equilibrated MD cells. Snapshots for the full LiTFSI concentration range (20–90 wt.% LiTFSI) are shown in Figure S12 (Supporting Information).

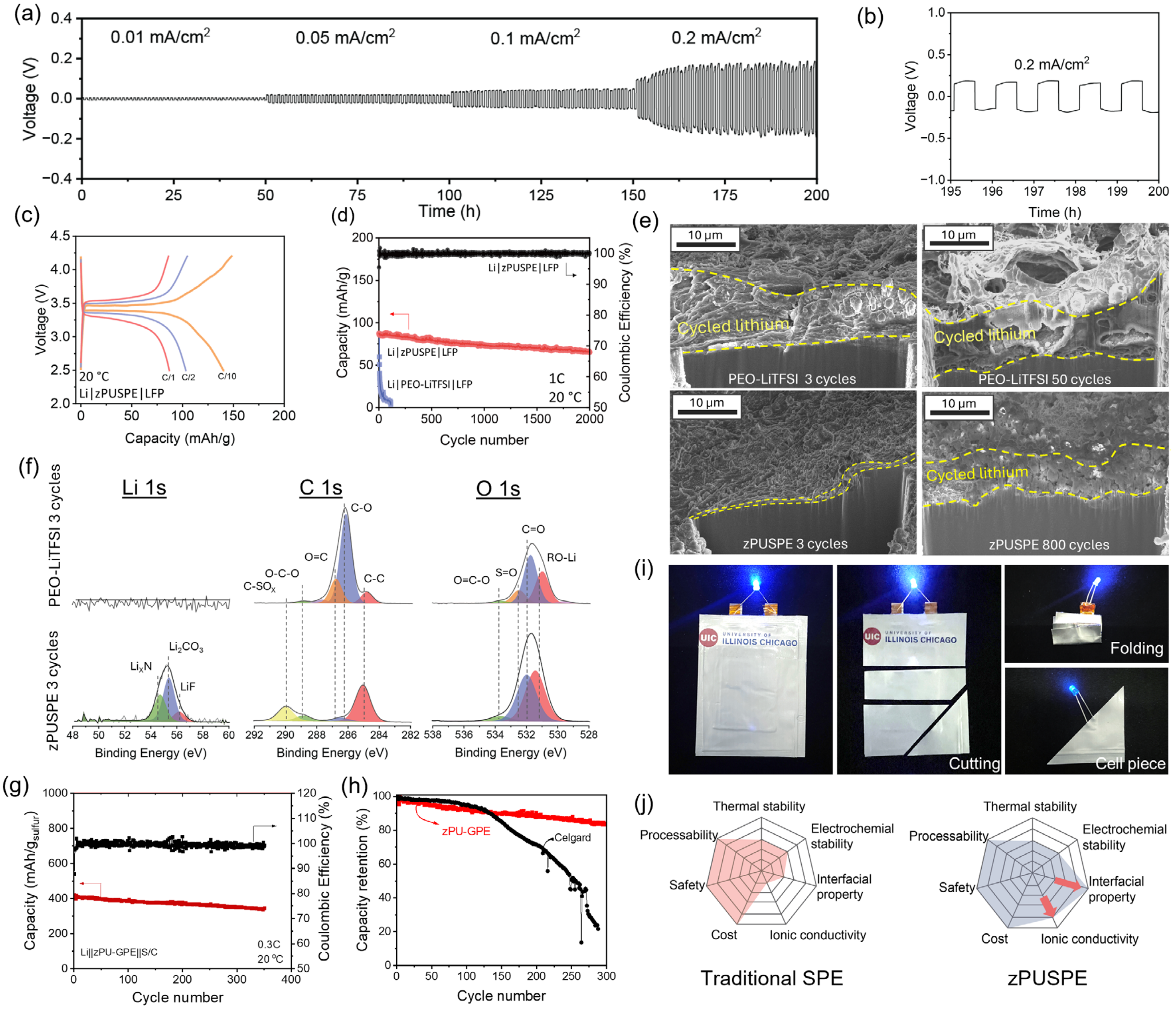

Figure 5. a) Strip-plate cycling of zPU-SPE in a lithium symmetric cell. Extended cycling results are shown in Figure S14 (Supporting Information). b) Enlarged figure of the strip-plate cycling under 0.2 mA cm^{-2}. c) Charge/discharge profiles of Li||zPU-SPE||LiFePO$_4$ coin cell at various C-rates. d) Discharge capacity and coulombic efficiency versus cycle number measured for a Li||zPU-SPE||LiFePO$_4$ coin cell at a 1C rate and 20 °C. e) PFIB-SEM images of the lithium surface after cycling in Li/zPU-SPE/LiFePO$_4$ coin cell and Li||PEO-LiTFSI||LiFePO$_4$ coin cell. f) Characterization of the SEI layer component on the cycled lithium metal anodes by XPS. g) Charge/discharge profiles of Li||zPU-GPE||S/C coin cell at 0.3C. h) Capacity retention curves of the Li/S coin cells with Celgard 2500 and zPU-GPE at a rate of 0.3C. i) Bending, cutting, and piercing experiment of a Li||zPU-SPE||LiFePO$_4$ soft pouch cell. j) Radar maps for the comparison of the zPU-SPE with traditional SPEs.

higher content of TFSI$^-$, which decreases as anions are solvated by zPU$^+$. This leads to enhanced Li$^+$ mobility and, hence, increased ionic conductivity.

2.4. Characterization of Battery Cell Performance with zPU-SPE

Nonuniform Li deposition and stripping during the cycling of ASSLBs can lead to unstable solid electrolyte interphase (SEI) layer formation and Li dendrite growth, which can subsequently trigger undesired side reactions and a reduction of Coulombic efficiency (CE). To investigate the compatibility of the zPU-SPE with Li anode and examine the stripping/plating behavior, we cycled Li-Li symmetric cell for 200 h with increasing current densities. As shown in **Figure 5a**, the voltage-time curve indicates that zPU-SPE remains stable under each current density, and its excellent long-term stability is further demonstrated in Figure S13 (Supporting Information). The typical 'arch' shape at the edge of the voltage profile, commonly observed in SPEs indicating dendritic and dead Li accumulation,[49] did not appear for the zPU-SPE (Figure 5b). In comparison, the Li-Li symmetric cell with traditional PEO-SPE could not be cycled at room temperature due to the large polarization at even low current density. Even at an elevated temperature of 60 °C, the cell with PEO-LiTFSI could cycle only at a low current density and shorted at 0.2 mA cm^{-2} (Figure S14, Supporting Information). The superior performance of zPU-SPE in contrast to PEO-SPE can be attributed to the good compatibility and interfacial contact between the zPU-SPE and Li electrodes, owing to the high adhesion energy of the zPU-SPE, which substantially reduces the interfacial resistance and generates a uniform Li^+ flux.

Figure 5c shows the charge-discharge profile at different C-rates. At C/10, C/2, and C/1 rates, the cell with the zPU-SPE exhibited discharge capacities of 148.2, 105, and 87.5 mAh/g, respectively. At a high C-rate of 1C, the zPU-SPE maintained 59% of the capacity achieved at a rate of C/10, which is comparable to previously reported polymer electrolytes. Due to the low activation energy of the ionic conductivity in the Arrhenius plot, the zPU-SPE can retain high ion-transport properties at ambient temperatures. The cycling performance and rate capability of the zPU-SPE were evaluated at 20 °C in a coin cell consisting of an LFP cathode and a Li anode (Figure 5d). The cell was cycled at a 1C charge-discharge rate and achieved a stable capacity of ≈87.5 mAh/g at the beginning of cycling. After 1000 cycles, the zPU-SPE exhibited a discharge capacity of 73.2 mAh/g with a capacity retention of 83.7%. Even after 2000 cycles, the cell can still maintain a 53.2 mAh/g capacity with a 76.1% capacity retention. In contrast, the capacity of the cell with PEO-SPE rapidly decreased to 30% of its initial capacity and failed after 100 cycles. Despite the development of various SPEs for ASSLBs in recent years, the reported cycling data of these cells are typically limited to 500 cycles, often only 100 cycles. However, a desired high-performance LIB should demonstrate at least 1000 cycles of cycling life with 80% capacity retention.[50] Benefiting from its good ion-transport properties and interfacial stability characteristics, the zPU-SPE achieved a cycling life with 80% capacity retention of 1670 cycles. Additionally, due to its low activation energy for the ionic conductivity (as shown in the Arrhenius plot in Figure 2f), the zPU-SPE can retain 87% of specific capacity at 0 °C (Figure S15, Supporting Information), a substantial improvement over most LIBs, which typically exhibit less than 80% capacity retention.

The stable cycling of ASSLBs with zPU-SPE was further studied by examining the Li morphology after cycling. As shown in the focused ion beam-SEM (FIB-SEM) analysis in Figure 5e, after three conditioning cycles under 0.1C, the cycled Li with PEO-LiTFSI electrolyte exhibited round-shaped Li plates with a total thickness of 9.3 µm. In contrast, the zPU-SPE produced a smooth Li deposit with a thin thickness of less than 1 µm. After an additional 50 cycles at 1C, the Li film with PEO-LiTFSI electrolyte developed a porous structure, with large voids at both the Li/substrate interface and within the bulk structure of the deposited Li, resulting in a total thickness of 9.6 ± 2.4 µm. Conversely, even after 800 cycles at 1C, the zPU-SPE exhibited a smooth, dendrite-free surface with densely packed, round-shaped Li particles and a thickness of 6.01 ± 1.1 µm. The low porosity and reduced thickness generated with zPU-SPE contribute to excellent structural integrity, increased CE, minimized volume changes, and reduced polarization during long-term cycling, partially explaining the outstanding cycling stability of ASSLBs with zPU-SPE.

XPS analysis was employed to further study the composition of the SEI layer on the cycled Li. As shown in Figure 5f, after the three formation cycles with PEO-LiTFSI under C/10, the Li surface was rich in carbon-based organic compounds with barely any inorganic components. In comparison, after three formation cycles under the same C-rate with zPU-SPE, inorganic species such as Li_xN, Li_2CO_3, and LiF were present. The more inorganic SEI layer in zPU-SPE could be attributed to the much higher inorganic salt loading (r = 5.6, 80 wt.% LiTFSI) compared to PEO-LiTFSI (30 wt.% LiTFSI). The inorganic Li compounds have a higher interfacial energy with Li metal, which can boost the diffusion of Li^+ through the SEI/Li interface and suppress the penetration of metallic Li dendrite through the SEI layer.[51] Also, the inorganic SEI layer has a higher modulus than the organic SEI layer, making it mechanically stronger to prevent the growth of Li dendrite.[52] Thus, the inorganic SEI layer from zPU-SPE contributed to more stable cycling and a longer lifetime in the ASSLB cell.

To assess the electrochemical performance of zPU-SPE beyond the ASSLB with an LFP cathode, lithium-sulfur (Li/S) batteries with zPU gel polymer electrolyte (zPU-GPE) were assembled, and their galvanostatic charge and discharge cycles were performed at 0.3C and 20 °C. As shown in Figure S16 (Supporting Information), the typical discharge profile is similar to that of a Li/S cell assembled with liquid electrolyte and a Celgard 2500 separator (Figure S17a, Supporting Information). The discharge curves exhibit two plateaus at 2.26 and 2.08 V. With an increasing number of cycles, these two plateaus were well maintained and remained even after 300 cycles. Although the discharge capacity of the Li/S cell with zPU-GPE in the first cycle (415 mAh/g) was lower than that of the liquid Li/S cell with Celgard (854 mAh/g), presumably due to higher membrane resistance, the capacity of the zPU-GPE cell was only slightly reduced to 350 mAh/g by the 300th cycle. Additionally, the Li/S cell with the zPU-GPE maintained a high CE (close to 100%). In comparison, the capacity of the liquid Li/S cell with the Celgard separator decreased more rapidly than that of the zPU-GPE cell, as evidenced by the charge-discharge curves for different cycle numbers (Figure S17b, Supporting Information). Eventually, the liquid Li/S cell failed after 300 cycles. As shown in the discharge retention curve of Figure 5h, despite the lower initial capacity of the Li/S cell with zPU-GPE, its decay rate was significantly lower than that of the Celgard 2500, largely due to the excellent ability of zPU membrane to suppress polysulfide crossover. Notably, after the capacity of the Li/S cell with zPU-GPE stabilizes at 130 cycles, the capacity decreases by only 1.3% over the next 170 cycles (0.07 mAh/g and 0.019% decay per cycle), and its capacity retention is 85% at 300 cycles.

Soft-package pouch cells were fabricated to explore the application of zPU-SPE and assess its safety. The safety of the Li||zPU-SPE||$LiFePO_4$ pouch cell was demonstrated at room temperature under several destructive conditions, as shown in Figure 5i. No short circuit occurred even after the pouch cell was cut or pierced. Notably, after three cuts and three piercings, a small portion of the remaining pouch cell continued to power the LED device, indicating that the reliability and safety of the zPU-SPE pouch cell were effectively maintained.

Figure 5j shows the radar maps comparing the performance of zPU-SPE to conventional SPE (comparison with IE is shown in Figure S18, Supporting Information). ASSLBs have garnered significant interest due to their safety benefits. Over the past decade, substantial advancements have been made in the study of electrolyte materials in ASSLBs. However, several challenges still remain. Although IEs offer excellent Li^+ conductivity, high cation selectivity (i.e., transference number), superior electrochemical and thermal stability, and the ability to limit dendrite penetration, their widespread use in LIBs is limited by their brittleness, as well as poor interfacial compatibility with electrodes.[3] In contrast, SPEs provide enhanced flexibility and ease of processing but have intrinsically low room-temperature ionic conductivity, as shown in Figure 5j. zPU-SPE combines the advantages of the traditional SPEs and IEs, while greatly enhancing the interfacial properties and self-healing functionality by incorporating ZI segments into the PU backbone. Thus, incorporating ZI groups offers a promising approach to developing next-generation SPEs to meet the demands of high-performance LIBs.

3. Conclusion

In summary, we introduce a multifunctional zPU-SPE that addresses the limitations of conventional SPE materials for ASSLBs. We demonstrated the capability of zPU-SPE to host 80 wt.% LiTFSI (r = 5.6) without phase separation. The ionic conductivity of zPU-SPE at 25 °C is 7.4×10^{-4} S cm^{-1} with a 0.44 of t_{Li+}, breaking the trade-off limitation of Li^+ selectivity and conductivity. The high surface energy of zPU-SPE (338.4 vs. 60.5 J m^{-2} of PEO) can effectively minimize interfacial resistance, and its outstanding elasticity and self-healing properties are attributed to dipole-dipole interactions and dense inter- and intramolecular hydrogen bonding. The ASSLB battery performance was demonstrated using a Li||SPE||$LiFePO_4$ cell cycled at 1C and 25 °C. The ASSLB cell with zPU-SPE demonstrated remarkable cycle stability, retaining 86% of its capacity after 1000 cycles and 76% after 2000 cycles with the $LiFePO_4$ cathode. Furthermore, Li/S cells assembled with zPU-GPE achieved 85% capacity retention after 300 cycles, all with ≈100% CE. We also conducted atomistic molecular modeling and SAXS to investigate Li salt dissolution, dissociation, Li^+ transport mechanisms, and the structural organization of the zPU-SPE matrix. The excellent electrochemical performance of zPU-SPE can be attributed to its good compatibility with electrodes, low charge transfer resistance at the electrode/electrolyte interface, and high Li^+ conductivity, strongly suggesting that zPU-SPE is a potential candidate for the development of high-performance SLBs.

4. Experimental Section

Materials: Diethanolamine (99%), polyethylene oxide (PEO; M_w = 600 000), poly(vinylidene fluoride) (PVDF; M_w = 534 000), and methanol (CH_3OH; ≥98%), were used as received from Sigma–Aldrich (Missouri, USA). 1,6 Diisocyanatohexane (HDI; ≥99%), ethyl acrylate (99.5%), diethyl ether (>95%), and an extra dry grade of dimethylformamide (DMF; 99.8%) were obtained from Acros Organics (Pittsburg, USA). Bis(trifluoromethane) sulfonimide lithium (LiTFSI; 99.95%) salt was purchased from Sigma–Aldrich (St. Louis; Missouri, USA) and stored in an Ar-filled glovebox with <0.1 ppm H_2O. 1,3- Dioxolane (DOL; 99.5%), and 1,2-Dimethoxy ethane (DME; ≥99%) solvents were received from Fisher Scientific (Ottawa, Canada) and subsequently dried over activated 3Å molecular sieves (Delta adsorbents; Illinois, USA). Li-coated Cu (53 µm thickness), and $LiFePO_4$ (LFP, granular particle size D(50): 1.5 µm) were purchased from MSE (Arizona, USA).

Fabrication of zPU-SPE: zPU [poly((diethanolamine ethyl acetate)-co-(1,6-diisocyanatohexane))] was synthesized based on the previously reported method.[53] Briefly, a ZI precursor and diol chain extender, diethanolamine ethyl acetate (DEAEA), was synthesized with 1:1.1 ratio of diethanolamine (Sigma–Aldrich, USA) and ethyl acrylate (Acros Organics, USA). zPU was synthesized via a one-pot reaction with a 1:1 ratio of DEAEA:1.6-diisocyanathohexane (Acros Organics, USA), followed by CH_3OH (Sigma–Aldrich, USA) quenching and purification in diethyl ether (Acros Organics, USA). The purified zPU solution was cast in PTFE dishes and dried in a vacuum oven at 100 °C to remove the residual solvent. After drying, the flat zPU film was peeled off from the PTFE dishes. The prepared zPU thin film was hydrolyzed in deionized (DI) water for 2 days to generate the ZI carboxybetaine groups, followed by 18 h of drying in a vacuum oven under 100 °C to remove residual water. zPU-SPEs were prepared in an Ar-filled glove box where the concentration of water was below 0.1 ppm. The hydrolyzed zPU thin film was impregnated with electrolyte solution composed of LiTFSI (Sigma–Aldrich, USA) in 1:1 vol% mixture of 1,3-dioxolane (DOL) and 1,2-dimethoxyethane (DME) (Fisher Scientific, Canada) solvent. After 18 h of equilibration, the prepared zPU film was dried in a vacuum oven at 80 °C for 18 h to remove DOL/DME, resulting in a thin zPU-SPE film electrolyte. The LiTFSI/zPU ratio was 5.6 unless specifically mentioned.

For the fabrication of zPU-GPE, a 4wt.% solution of zPU in DMF was homogeneously infiltrated into microporous polyethylene (PE) membrane support with 16 µm thickness and 80% porosity. The infiltration was carried out under vacuum at room temperature for 6 h. Subsequently, the membrane was dried in a conventional oven at 50 °C for 5 h, followed by further drying in a vacuum oven at 80 °C for 18 h. The reinforced zPU membrane was subjected to hydrolysis in DI water for 2 days, followed by drying in a vacuum oven at 80 °C for 24 h. The hydrolyzed zPU membrane was immersed in 1M LiTFSI + 3 wt.% $LiNO_3$ in DOL-DME (1:1 v/v) electrolyte solution for 18 h. Excess liquid electrolyte was removed using Kimwipes to obtain zPU-GPE with a thickness of approximately 17 µm.

Physicochemical Characterization: Scanning electron microscopy and energy dispersive X-ray spectroscopy (SEM-EDS) (JSM-IT500HR FESEM, JEOL) analysis were carried out to study the LiTFSI distribution in zPU-SPE and the cross-section morphology of battery cell components. The thermal stability of zPU-SPE was investigated using a thermogravimetric analysis (TGA) (Pyris 1, PerkinElmer) with a temperature increase rate of 5 °C min^{-1}. The chemical composition and salt-polymer association between LiTFSI and zPU were evaluated by using X-ray photoelectron spectroscopy (XPS) (AXIS-165, Kratos) and an attenuated total reflectance Fourier-transform infrared spectroscopy (ATR-FTIR) (Vertex 80, Bruker). Each measurement was recorded in the mid-infrared region with a resolution of 4 cm^{-1}. Mechanical tensile stress and surface adhesion experiments were carried out using a compact bench testing machine (EZ-Test, Shimadzu) with a rate of 1 mm s^{-1}. Surface adhesion energy was calculated using a reported method,[22c] where the sample was sandwiched between two Li-coated copper foils and peeled by the universal mechanical tester at 1 cm min^{-1} speed. The adhesion energy was calculated from the peeling force per width of the sample (Figure S4, Supporting Information).

Battery Fabrication and Electrochemical Characterization: The ionic conductivity was measured by Electrochemical Impedance Spectroscopy (EIS) with a Swagelok-type stainless steel symmetric cell through a potentiostat (Autolab, Metrohm). The intercept of the Nyquist plot with the x-axis was used as the resistance for calculating the ionic conductivity. For Li^+ transference number (t_{Li+}) calculations, the method by Bruce and co-workers was followed, employing DC polarization combined with impedance spectroscopy in a lithium symmetric cell at an applied voltage of 20 mV.[54] Linear sweep voltammetry (LSV) experiments were performed at a scan rate of 1 mV s^{-1}, with lithium as the counter electrode and stainless steel as the working electrode. For lithium stripping-plating tests, symmetric lithium cells were assembled with copper foil as the current collectors. Cells were charged and discharged at predetermined current densities for a period of 30 min each.

LB cell testing in an LFP||zPU-SPE||Li configuration was conducted using stainless steel CR2025 coin cells and 3450 pouch cells. LFP cathodes were fabricated following a previously reported protocol.[33c] PVDF, used as a binder, was first dissolved in NMP and stirred overnight. Subsequently, LFP particles, conductive carbon, and the PVDF-NMP solution

(LFP:carbon:PVDF = 80:10:10 wt.%) were combined and ball-milled with zirconia balls to ensure homogeneous mixing. The resulting slurry was then cast onto aluminum foil, dried, and calendered prior to use.

All the cells were assembled in an Ar-filled glovebox with <0.1 ppm water level. For the coin cells, electrodes and zPU-SPE were cut into circular discs with 3/8 inch and 1/2 inch diameters, respectively. For the pouch cells, cathode, Li-coated copper anode, and zPU-SPE were cut to 34 mm × 50 mm, 36 mm × 52 mm, and 40 mm × 55 mm, respectively. The active loading of the LFP cathode was 1.3 mg cm^{-2}. The cathode was infiltrated with zPU-SPE as a catholyte. Specifically, purified zPU solution was cast onto the LFP cathode, allowing the solution to fill the cathode pores. After vacuum drying at 80 °C, the zPU polymer-filled cathode underwent hydrolyzation, salt impregnation, and further drying, following the zPU-SPE fabrication process described in Section Fabrication of zPU-SPE. The lithium anode has a thickness of 50 µm. The cells were preconditioned by three cycles at a rate of C/20 before extended cycling testing. The galvanostatic charge-discharge cycling measurements were conducted using an eight-channel battery analyzer (CT-4008-5V10mA, Neware) at 20 °C. The charging and discharging tests used cutoff voltages of 4.1 V and 2.5 V, respectively.

For the fabrication of Li||electrolyte||S/C coin cell, the reinformed zPU membrane was placed between a Li—Cu anode (MSE Supplies, USA) and a commercial S/C cathode (NexTech Batteries, USA). A Celgard 2500 membrane saturated in liquid electrolyte was used as a control. For all cells, the S/C cathode was dried in a vacuum oven at 60 °C for 24 h and prewetted with 15 µL of a 1 M LiTFSI + 3 wt.% $LiNO_3$ electrolyte solution in DOL-DME (1:1 v/v). The mass loading of sulfur in the S/C cathode was 3.25 mg cms^{-2}. All cells were assembled in an argon-filled glovebox (<0.1 ppm H_2O). The assembled Li/S coin cells were preconditioned for two cycles at a rate of 0.03C and 0.06C, followed by extended cycling at 0.3C.

Molecular Dynamics Simulation: For classical molecular dynamics simulation (MD), the zPU-SPE systems composing LiTFSI salt with a LiTFSI/ZI ratio of 0.2–5.6 (20 – 90 wt.%) were assembled. The non-polarizable all-atomic OPLS(-AA), "Optimized Potentials for Liquid Simulations," force field (as available in the Gromacs simulation package database),[55,56] was utilized to adjust most of the intra- and intermolecular potential parameters, describing covalent terms within bond stretching, angle bending and dihedral angle torsion along the covalent bond, and non-covalent terms represented by the van der Waals. A chain length of 20 zPU monomers was selected. Each initial system was generated by Packmol[57] and placed into an orthorhombic box with 3D periodic boundary conditions. All MD simulations were carried out using Gromacs, v2016.3. The equations of motion were integrated using the leap-frog algorithm[58] with a time-step of 2×10^{-6} ns. The zPU-SPE systems were energy-minimized using the steepest descent algorithm, followed by the same stepwise isothermal-isobaric and canonical equilibration protocol reported for a similar SPE system[59] by applying Berendsen thermostat and barostat,[60] with coupling constants of 3×10^{-4} and 5×10^{-4} ns for initial steps, and velocity-rescaling[61] thermostat and Parrinello-Rahman barostat[62] for the last steps. During the production stage, the thermostat was substituted by the Nose-Hoover one (8×10^{-4} ns).[63] The structural properties presented in this work were further enhanced by Travis code,[64] v052121.

Raman Spectroscopy: The samples were placed across microscope slides with carbon tape on the edges, and a quartz slide was placed and stuck on top to create a sandwich configuration. Gorilla tape was then used on the edges of the slides to ensure the system was fully sealed. A confocal Raman microscope (NRS-5100, JASCO) mapped out a 3 × 3 array of points to collect each sample for 9 different regions. 5–9 spectra were then taken for each sample and averaged, followed by background subtraction of the quartz spectrum. The data was collected with a 532 nm laser at 5 accumulations for an exposure of 10 s per spectrum.

Surface Characterizations of Lithium: Li metal electrodes were harvested from the coin cells and then washed with DME to remove the residual polymer electrolyte in the Ar-filled glovebox (H_2O and O_2 <0.1ppm). XPS was performed with the X-ray photoelectron spectrometer (XPS) (Kratos Axis Ultra, Shimadzu) with an aluminum anode source at 10kV and a spot size of 300 mm x 700 mm during acquisition. The chamber pressure was kept at $<10^{-8}$ torr during all measurements. Fittings of the XPS spectra were obtained using CasaXPS software to determine the surface species using a Shirley background and were based on the reference C—C bond at 284.8 eV.

For PFIB-SEM measurement, the samples were mounted on Ted Pella SEM stubs and placed in heat-sealed aluminum bags before being transferred into the Plasma FIB-SEM (Helios G4, Thermo Scientific). A Xenon ion beam with a voltage of 30 kV and a beam current of 200 nA was used to create cross-sections of the Li metal anode. The cross sections were polished with an ion beam current of 60 nA. The SEM images of the cross sections were taken using the TLD lens detector at 5kV and 0.1nA.

Small Angle X-Ray Scattering and Wide Angle X-Ray Scattering: Small/wide angle X-ray scattering (SAXS/WAXS) experiments were conducted at the 12ID-B station of the Advanced Photon Source at Argonne National Laboratory with an X-ray energy of 13.3 keV and a Pilatus 2M detector located ≈2 m from the sample. All samples were loaded into the quartz capillary and sealed. All the measurements were performed at room temperature.

Destructive Test of Pouch Cell: To evaluate the safety and reliability of zPU-SPE under extreme conditions, destructive tests were conducted on soft-package pouch cells. The pouch cells were first fabricated and cycled for two formation cycles. Afterward, they were connected to a blue LED (3.0–3.2 V) as a visual indicator of functionality. The pouch cells were then subjected to mechanical stress, including folding, cutting with scissors, and piercing with a blade, while their performance was continuously monitored. The LED remained illuminated throughout the tests, confirming that the pouch cell did not short-circuit despite the inflicted damage.

Supporting Information

Supporting Information is available from the Wiley Online Library or from the author.

Acknowledgements

The majority of this work was financially supported by the National Science Foundation (NSF, Grant No. CBET-2224253). The authors thank Dr. Fengyuan Shi from the Electron Microscopy Core of the Research Resources Center at UIC for her expert assistance in conducting the XPS measurement and analysis. PD and JLS thank the Department of Education (Grant no. P200A21004) and the NSF (Grant no. CBET-2044386) for support for Raman spectroscopy measurements performed at the University of Notre Dame Materials Characterization Facility. TL was grateful for the support from the NSF (Grant No. 2208972, 2120559, and 2323117). VK and AN were grateful for the computational resources provided on Bebop, a high-performance computing cluster operated by the Laboratory Computing Resource Center at Argonne National Laboratory (ANL). This research also used resources of the Advanced Photon Source, a U.S. Department of Energy (DOE) Office of Science User Facility operated for the DOE Office of Science by ANL under Contract No. DE-AC02-06CH11357.

Conflict of Interest

The authors declare no conflict of interest.

Data Availability Statement

The data that support the findings of this study are available from the corresponding author upon reasonable request.

Keywords

all solid-state lithium battery, ion-solvation structure, lithium–sulfur battery, polymer-in-salt electrolyte, zwitterionic polyurethane

Received: December 2, 2024
Revised: April 22, 2025
Published online:

---

[1] a) M. Armand, J. M. Tarascon, *Nature* **2008**, *451*, 652; b) A. Wang, S. Geng, Z. Zhao, Z. Hu, J. Luo, *Adv. Funct. Mater.* **2022**, *32*, 2201861.

[2] Z. Lv, Y. Tang, S. Dong, Q. Zhou, G. Cui, *Chem. Eng. J.* **2021**, *430*, 132659.

[3] X. Yu, A. Manthiram, *Energy Storage Mater.* **2021**, *34*, 282.

[4] R. Chen, Q. Li, X. Yu, L. Chen, H. Li, *Chem. Rev.* **2020**, *120*, 6820.

[5] a) D. Zhou, D. Shanmukaraj, A. Tkacheva, M. Armand, G. Wang, *Chem* **2019**, *5*, 2326; b) L. Zhang, S. Wang, Q. Wang, H. Shao, Z. Jin, *Adv. Mater.* **2023**, *35*, 2303355.

[6] J. Zhang, L. Yue, P. Hu, Z. Liu, B. Qin, B. Zhang, Q. Wang, G. Ding, C. Zhang, X. Zhou, J. Yao, G. Cui, L. Chen, *Sci. Rep.* **2015**, *4*, 6272.

[7] a) M. W. Schulze, L. D. McIntosh, M. A. Hillmyer, T. P. Lodge, *Nano Lett.* **2014**, *14*, 122; b) D.-G. Kim, J. Shim, J. H. Lee, S.-J. Kwon, J.-H. Baik, J.-C. Lee, *Polymer* **2013**, *54*, 5812; c) F. Croce, S. Sacchetti, B. Scrosati, *J. Power Sources* **2006**, *161*, 560.

[8] M. Yao, Q. Ruan, T. Yu, H. Zhang, S. Zhang, *Energy Storage Mater.* **2022**, *44*, 93.

[9] a) H. Li, Y. Du, X. Wu, J. Xie, F. Lian, *Adv. Funct. Mater.* **2021**, *31*, 2103049; b) L. Mathies, D. Diddens, D. Dong, D. Bedrov, H. Leipner, *Solid State Ionics* **2020**, *357*, 115497.

[10] Z. Song, F. Chen, M. Martinez-Ibañez, W. Feng, M. Forsyth, Z. Zhou, M. Armand, H. Zhang, *Nat. Commun.* **2023**, *14*, 4884.

[11] H. Wu, P. Gao, H. Jia, L. Zou, L. Zhang, X. Cao, M. H. Engelhard, M. E. Bowden, M. S. Ding, J. Hu, *ACS Appl. Mater. Interfaces* **2021**, *13*, 31583.

[12] H. Gao, N. S. Grundish, Y. Zhao, A. Zhou, J. B. Goodenough, *Energy Mater. Adv.* **2021**, *2021*, 1932952.

[13] W. Liu, C. Yi, L. Li, S. Liu, Q. Gui, D. Ba, Y. Li, D. Peng, J. Liu, *Angew. Chem.* **2021**, *133*, 13041.

[14] a) Z. Li, Q. Xia, L. Liu, G. Lei, Q. Xiao, D. Gao, X. Zhou, *Electrochim. Acta* **2010**, *56*, 804; b) I. L. Johansson, C. Sangeland, T. Uemiya, F. Iwasaki, M. Yoshizawa-Fujita, D. Brandell, J. Mindemark, *ACS Appl. Energy Mater.* **2022**, *5*, 10002; c) F. Makhlooghiazad, L. A. O'Dell, L. Porcarelli, C. Forsyth, N. Quazi, M. Asadi, O. Hutt, D. Mecerreyes, M. Forsyth, J. M. Pringle, *Nat. Mater.* **2022**, *21*, 228; d) Y. Wang, S. Geng, G. Yan, X. Liu, X. Zhang, Y. Feng, J. Shi, X. Qu, *ACS Appl. Energy Mater.* **2022**, *5*, 2495.

[15] L. Mi, S. Jiang, *Angew. Chem. Int. Ed. Engl.* **2014**, *53*, 1746.

[16] a) F. Mo, Z. Chen, G. Liang, D. Wang, Y. Zhao, H. Li, B. Dong, C. Zhi, *Adv. Energy Mater.* **2020**, *10*, 2000035; b) J. Cardoso, A. Huanosta, O. Manero, *Macromolecules* **1991**, *24*, 2890; c) C. Tiyapiboonchaiya, J. M. Pringle, J. Sun, N. Byrne, P. C. Howlett, D. R. Macfarlane, M. Forsyth, *Nat. Mater.* **2004**, *3*, 29; d) X. Peng, H. Liu, Q. Yin, J. Wu, P. Chen, G. Zhang, G. Liu, C. Wu, Y. Xie, *Nat. Commun.* **2016**, *7*, 11782; e) Z. Zhang, P. Zhang, Z. Liu, B. Du, Z. Peng, *ACS Appl. Mater. Interfaces* **2020**, *12*, 11635; f) C. Liu, S. Wang, X. Wu, S. Xiao, C. Liu, H. Cai, W. Y. Lai, *Adv. Funct. Mater.* **2024**, *34*, 2307248.

[17] a) F. Lu, G. Li, Y. Yu, X. Gao, L. Zheng, Z. Chen, *Chem. Eng. J.* **2020**, *384*, 123237; b) G. Guzmán, D. Nava, J. Vazquez-Arenas, J. Cardoso, J. Alvarez-Ramirez, *Solid State Ionics* **2018**, *320*, 45; c) J. Cardoso, O. Soria-Arteche, G. Vázquez, O. Solorza, I. González, *J. Phys. Chem. C* **2010**, *114*, 14261; d) S. D. Jones, H. Nguyen, P. M. Richardson, Y.-Q. Chen, K. E. Wyckoff, C. J. Hawker, R. J. Clément, G. H. Fredrickson, R. A. Segalman, *ACS Cent. Sci.* **2022**, *8*, 169.

[18] a) J. Zhu, Z. Zhang, S. Zhao, A. S. Westover, I. Belharouak, P. F. Cao, *Adv. Energy Mater.* **2021**, *11*, 2003836; b) M. E. Taylor, D. Clarkson, S. G. Greenbaum, M. J. Panzer, *ACS Appl. Polym. Mater* **2021**, *3*, 2635.

[19] C. D. D. Sundari, J. Karunawan, S. P. Santosa, I. M. Arcana, F. Iskandar, *ACS Appl. Polym. Mater* **2023**, *5*, 6817.

[20] B.-X. Cheng, W.-C. Gao, X.-M. Ren, X.-Y. Ouyang, Y. Zhao, H. Zhao, W. Wu, C.-X. Huang, Y. Liu, X.-Y. Liu, *Polym. Test.* **2022**, *107*, 107489.

[21] J. Bao, C. Tao, R. Yu, M. Gao, Y. Huang, C. Chen, *J. Appl. Polym. Sci.* **2017**, *134*, 45554.

[22] a) B. Xu, Z. Liu, J. Li, X. Huang, B. Qie, T. Gong, L. Tan, X. Yang, D. Paley, M. Dontigny, *Nano Energy* **2020**, *67*, 104242; b) X. He, A. Ye, X. Fu, W. Yang, Y. Wang, *Macromolecules* **2022**, *55*, 7117; c) M. J. Lee, J. Han, K. Lee, Y. J. Lee, B. G. Kim, K.-N. Jung, B. J. Kim, S. W. Lee, *Nature* **2022**, *601*, 217.

[23] Y. Guo, X. Qu, Z. Hu, J. Zhu, W. Niu, X. Liu, *J. Mater. Chem. A* **2021**, *9*, 13597.

[24] a) C.-T. Yang, Y.-X. Lin, B. Li, X. Xiao, Y. Qi, *ACS Appl. Mater. Interfaces* **2020**, *12*, 51007; b) M. H. Ryou, D. J. Lee, J. N. Lee, Y. M. Lee, J. K. Park, J. W. Choi, *Adv. Energy Mater.* **2012**, *2*, 645.

[25] a) L. Gong, L. Xiang, J. Zhang, J. Chen, H. Zeng, *Langmuir* **2019**, *35*, 15914; b) J. Wang, L. Wang, C. Wu, X. Pei, Y. Cong, R. Zhang, J. Fu, *ACS Appl. Mater. Interfaces* **2020**, *12*, 46816; c) M. Ebadi, C. Marchiori, J. Mindemark, D. Brandell, C. M. Araujo, *J. Mater. Chem. A* **2019**, *7*, 8394.

[26] Y. H. Jo, S. Li, C. Zuo, Y. Zhang, H. Gan, S. Li, L. Yu, D. He, X. Xie, Z. Xue, *Macromolecules* **2020**, *53*, 1024.

[27] Z. Sun, J. Wu, H. Yuan, J. Lan, Y. Yu, Y. Zhu, X. Yang, *Mater. Today Energy* **2022**, *24*, 100939.

[28] A. J. D'Angelo, M. J. Panzer, *Chem. Mater.* **2019**, *31*, 2913.

[29] a) B. Zhou, Y. H. Jo, R. Wang, D. He, X. Zhou, X. Xie, Z. Xue, *J. Mater. Chem. A* **2019**, *7*, 10354; b) H. Gan, Y. Zhang, S. Li, L. Yu, J. Wang, Z. Xue, *ACS Appl. Energy Mater.* **2020**, *4*, 482.

[30] Y. Yang, W. Yang, H. Yang, H. Zhou, *Escience* **2023**, *3*, 100170.

[31] L. Seidl, R. Grissa, L. Zhang, S. Trabesinger, C. Battaglia, *Adv. Mater. Interfaces* **2022**, *9*, 2100704.

[32] S. B. Aziz, T. J. Woo, M. Kadir, H. M. Ahmed, *J. Sci.: Adv. Mater. Devices* **2018**, *3*, 1.

[33] a) J. Bao, X. Qu, G. Qi, Q. Huang, S. Wu, C. Tao, M. Gao, C. Chen, *Solid State Ionics* **2018**, *320*, 55; b) B. Cong, Y. Song, N. Ren, G. Xie, C. Tao, Y. Huang, G. Xu, J. Bao, *Mater. Des.* **2018**, *142*, 221; c) N. Wu, Y. R. Shi, S. Y. Lang, J. M. Zhou, J. Y. Liang, W. Wang, S. J. Tan, Y. X. Yin, R. Wen, Y. G. Guo, *Angew. Chem., Int. Ed.* **2019**, *58*, 18146; d) J. Bao, G. Shi, C. Tao, C. Wang, C. Zhu, L. Cheng, G. Qian, C. Chen, *J. Power Sources* **2018**, *389*, 84.

[34] A. J. D'Angelo, M. J. Panzer, *Adv. Energy Mater.* **2018**, *8*, 1801646.

[35] a) D. M. Pesko, S. Sawhney, J. Newman, N. P. Balsara, *J. Electrochem. Soc.* **2018**, *165*, A3014; b) Q. J. Meisner, T. Rojas, T. Glossmann, A. Hintennach, Q. Liu, J. Cao, P. C. Redfern, A. T. Ngo, L. A. Curtiss, Z. Zhang, *J. Electrochem. Soc.* **2020**, *167*, 070528.

[36] a) C. Brissot, M. Rosso, J.-N. Chazalviel, S. Lascaud, *J. Power Sources* **1999**, *81*, 925; b) M. D. Tikekar, L. A. Archer, D. L. Koch, *J. Electrochem. Soc.* **2014**, *161*, A847.

[37] M. D. Galluzzo, J. A. Maslyn, D. B. Shah, N. P. Balsara, *J. Chem. Phys.* **2019**, *151*, 020901.

[38] a) M. Liu, B. Jin, Q. Zhang, X. Zhan, F. Chen, *J. Alloys Compd.* **2018**, *742*, 619; b) A. J. D'Angelo, M. J. Panzer, *J. Phys. Chem. B* **2017**, *121*, 890.

[39] X. Shan, S. Zhao, M. Ma, Y. Pan, Z. Xiao, B. Li, A. P. Sokolov, M. Tian, H. Yang, P.-F. Cao, *ACS Appl. Mater. Interfaces* **2022**, *14*, 56110.

[40] B. A. Fortuin, J. Otegi, J. M. López del Amo, S. R. Peña, L. Meabe, H. Manzano, M. Martínez-Ibañez, J. Carrasco, *Phys. Chem. Chem. Phys.* **2023**, *25*, 25038.

[41] a) X. Liu, L. Fang, X. Lyu, R. E. Winans, T. Li, *Chem. Mater.* **2023**, *35*, 9821; b) X. Liu, V. Koverga, H. T. Nguyen, A. T. Ngo, T. Li, *Appl. Phys. Rev.* **2024**, *11*, 021307; c) K. Qian, S. Seifert, R. E. Winans, T. Li, *Energy Fuels* **2021**, *35*, 19849.

[42] H. Zhang, M. Armand, *Isr. J. Chem.* **2021**, *61*, 94.

[43] D. M. Seo, P. D. Boyle, R. D. Sommer, J. S. Daubert, O. Borodin, W. A. Henderson, *J. Phys. Chem. B* **2014**, *118*, 13601.
[44] O. Borodin, J. Self, K. A. Persson, C. Wang, K. Xu, *Joule* **2020**, *4*, 69.
[45] G. A. Giffin, *Nat. Commun.* **2022**, *13*, 5250.
[46] a) M. Yoshizawa, M. Hirao, K. Ito-Akita, H. Ohno, *J. Mater. Chem.* **2001**, *11*, 1057; b) N. Byrne, P. C. Howlett, D. R. MacFarlane, M. Forsyth, *Adv. Mater.* **2005**, *17*, 2497.
[47] a) K. Kimura, J. Motomatsu, Y. Tominaga, *J. Phys. Chem. C* **2016**, *120*, 12385; b) X. Wang, F. Chen, G. M. Girard, H. Zhu, D. R. MacFarlane, D. Mecerreyes, M. Armand, P. C. Howlett, M. Forsyth, *Joule* **2019**, *3*, 2687; c) K. Pożyczka, M. Marzantowicz, J. Dygas, F. Krok, *Electrochim. Acta* **2017**, *227*, 127.
[48] H. Wu, P. Gao, H. Jia, L. Zou, L. Zhang, X. Cao, M. H. Engelhard, M. E. Bowden, M. S. Ding, J. Hu, D. Hu, S. D. Burton, K. Xu, C. Wang, J.-G. Zhang, W. Xu, *ACS Appl. Mater. Interfaces* **2021**, *13*, 31583.
[49] H. Wang, Y. Yang, C. Gao, T. Chen, J. Song, Y. Zuo, Q. Fang, T. Yang, W. Xiao, K. Zhang, *Nat. Commun.* **2024**, *15*, 2500.
[50] A. Masias, J. Marcicki, W. A. Paxton, *ACS Energy Lett.* **2021**, *6*, 621.
[51] S. Liu, X. Ji, N. Piao, J. Chen, N. Eidson, J. Xu, P. Wang, L. Chen, J. Zhang, T. Deng, *Angew. Chem., Int. Ed.* **2021**, *60*, 3661.
[52] X. B. Cheng, R. Zhang, C. Z. Zhao, F. Wei, J. G. Zhang, Q. Zhang, *Adv. Sci.* **2016**, *3*, 1500213.
[53] K. Wang, T. Arado, A. Huner, H. Seol, X. Liu, H. Wang, L. Hassan, K. Suresh, S. Kim, G. Cheng, *Biomater. Sci.* **2022**, *10*, 2892.
[54] P. G. Bruce, C. A. Vincent, *J. Electroanal. Chem. Interfacial Electrochem.* **1987**, *225*, 1.
[55] a) H. J. C. Berendsen, D. van der Spoel, R. van Drunen, *Comput. Phys. Commun.* **1995**, *91*, 43; b) E. Lindahl, B. Hess, D. van der Spoel, *Molecular modeling annual* **2001**, *7*, 306; c) D. Van Der Spoel, E. Lindahl, B. Hess, G. Groenhof, A. E. Mark, H. J. C. Berendsen, *J. Comput. Chem.* **2005**, *26*, 1701; d) B. Hess, C. Kutzner, D. van der Spoel, E. Lindahl, *J. Chem. Theory Comput.* **2008**, *4*, 435; e) S. Pronk, S. Páll, R. Schulz, P. Larsson, P. Bjelkmar, R. Apostolov, M. R. Shirts, J. C. Smith, P. M. Kasson, D. van der Spoel, B. Hess, E. Lindahl, *Bioinformatics* **2013**, *29*, 845; f) M. J. Abraham, T. Murtola, R. Schulz, S. Páll, J. C. Smith, B. Hess, E. Lindahl, *SoftwareX* **2015**, *1–2*, 19; g) S. Páll, M. J. Abraham, C. Kutzner, B. Hess, E. Lindahl, presented at *Solving Software Challenges for Exascale*, Springer, Cham, **2015**.
[56] a) W. L. Jorgensen, J. Tirado-Rives, *J. Am. Chem. Soc.* **1988**, *110*, 1657; b) W. L. Jorgensen, D. S. Maxwell, J. Tirado-Rives, *J. Am. Chem. Soc.* **1996**, *118*, 11225.
[57] L. Martínez, R. Andrade, E. G. Birgin, J. M. Martínez, *J. Comput. Chem.* **2009**, *30*, 2157.
[58] R. W. Hockney, S. P. Goel, J. W. Eastwood, *J. Comput. Phys.* **1974**, *14*, 148.
[59] W. Zhang, V. Koverga, S. Liu, J. Zhou, J. Wang, P. Bai, S. Tan, N. K. Dandu, Z. Wang, F. Chen, J. Xia, H. Wan, X. Zhang, H. Yang, B. L. Lucht, A.-M. Li, X.-Q. Yang, E. Hu, S. R. Raghavan, A. T. Ngo, C. Wang, *Nat. Energy* **2024**, *9*, 386.
[60] H. J. C. Berendsen, J. P. M. Postma, W. F. van Gunsteren, A. DiNola, J. R. Haak, *J. Chem. Phys.* **1984**, *81*, 3684.
[61] G. Bussi, D. Donadio, M. Parrinello, *J. Chem. Phys.* **2007**, *126*, 014101.
[62] M. Parrinello, A. Rahman, *J. Appl. Phys.* **1981**, *52*, 7182.
[63] a) W. G. Hoover, A. J. C. Ladd, B. Moran, *Phys. Rev. Lett.* **1982**, *48*, 1818; b) S. Nosé, *J. Chem. Phys.* **1984**, *81*, 511; c) S. Nosé, *Mol. Phys.* **1984**, *52*, 255.
[64] a) M. Brehm, B. Kirchner, *J. Chem. Inf. Model.* **2011**, *51*, 2007; b) M. Brehm, M. Thomas, S. Gehrke, B. Kirchner, *J. Chem. Phys.* **2020**, *152*, 164105.